Research Square

Preprints are preliminary reports that have not undergone peer review.
They should not be considered conclusive, used to inform clinical practice,
or referenced by the media as validated information.

Visible Colorimetric Dosimetry of UV and Ionizing Radiations by a Dual-Module Photochromic Nanocluster

Huangjie Lu
Key Laboratory of Interfacial Physics and Technology, Shanghai Institute of Applied Physics, Chinese Academy of Sciences

Jian Xie
State Key Laboratory of Radiation Medicine and Protection, Soochow University

Xin-Xu Wang
Key Laboratory of Functional Inorganic Material Chemistry (Ministry of Education), School of Chemistry and Materials Science, Heilongjiang University

Yaxing Wang
Soochow University

Zi-Jian Li
Shanghai Institute of Applied Physics https://orcid.org/0000-0002-3887-0234

Kariem Diefenbach
FSU

Qing-Jiang Pan
Key Laboratory of Functional Inorganic Material Chemistry (Ministry of Education), School of Chemistry and Materials Science, Heilongjiang University

Jian-Qiang Wang
Shanghai Institute of Applied Physics https://orcid.org/0000-0003-4123-7592

Shuao Wang (shuaowang@suda.edu.cn)
State Key Laboratory of Radiation Medicine and Protection, Soochow University

Jian Lin
Key Laboratory of Interfacial Physics and Technology, Shanghai Institute of Applied Physics, Chinese Academy of Sciences

---

Article

Keywords: Radiation dosimeters, dosimetry, UV and ionizing radiations, dual-module photochromic nanocluster

Posted Date: October 2nd, 2020

Loading [MathJax]/jax/output/CommonHTML/jax.js

DOI: https://doi.org/10.21203/rs.3.rs-81902/v1

License: This work is licensed under a Creative Commons Attribution 4.0 International License.
Read Full License

Version of Record: A version of this preprint was published at Nature Communications on May 14th, 2021. See the published version at https://doi.org/10.1038/s41467-021-23190-0.

Loading [MathJax]/jax/output/CommonHTML/jax.js

Abstract

Radiation dosimeters displaying conspicuous response of irradiance are highly desirable over the recent decade owing to the growing demand of monitoring high-energy radiation and environmental exposure. Herein, we present the first case of dosimetry based on a discrete nanocluster by judicious incorporating heavy Th_6 polynuclear centers as radiation attenuator and organic linkers as photo-responsive sensor to enhance chromic response. Rather unusual dual-module photochromic transitions upon multiple external stimuli including UV, β-ray, and γ-ray are integrated into this single material. The striking color change, and more significantly, the visible chromic transition of luminescence in response to accumulating radiation dose allow an on-site quantitative platform for naked-eye detection of ionization radiations over a broad range (1–80 kGy). SC-XRD and DFT calculations revealed that the dual-module photochromism can be attributed to a unique π(TPC)→π*(TPC) intermolecular charge transfer (IeMCT) driven by enhanced π-π stacking interaction between the adjacent TPC moieties upon irradiations.

Introduction

Developing new radiation dosimeters has been a very active research area of inquiry for the past decades, owning to the cumulative demands of such materials in multifarious fields, including nuclear industry, medical radiation, cosmic exploration, and instrumentation calibration.[1, 2, 3, 4, 5, 6] Quantitatively detection of a radiation dose usually occurs by converting incident energy to a low-energy photon response, electronic current, or threshold voltage by radiation detectors.[7] These types of dosimeters, e.g. ionization chambers, thermoluminescent dosimeters (TLDs), diodes, and semiconductors, are typically coupled to readout instruments such as a photomultiplier and electrometer, or even spectrophotometer which is only available in well-equipped laboratories, to obtain quantitative information.[8, 9, 10, 11, 12] On the other hand, radiochromic films allow for direct readout and onsite assessment of radiation exposure via visible color change.[13] However, only qualitative or semi-quantitative characterization of radiation can be accomplished without the assistance of a spectrophotometer.[14] Therefore, the quest for developing new absolute radiation dosimeters that provide a more straightforward route for dosimetry of ionizing radiations remains ongoing.

Metal-organic complexes featuring photoinduced changes of electronic properties, photochromism and photoluminescence (PL), represent a promising dosimetry platform for colorimetric visualization of ionizing radiation.[15, 16, 17] The incorporation of a metal center with a high atomic number (Z) endows the material with increased radiation attenuation efficiency.[18, 19] Furthermore, coordinating linkers decorated with a photoactive ligand, such as pyridine, viologen, and azobenzene, allows for charge-transfer and formation of radical species upon irradiation, inducing visualizable color transitions. [20, 21, 22, 23, 24] Metal-organic complexes featuring ionizing radiation induced photochromism are uncommon; systems showing photochromically modulated luminescence are even rarer.[25, 26, 27] In addition, the PL modulations of these materials are limited to simple on/off switching with coloring/bleaching behaviors,

Loading [MathJax]/jax/output/CommonHTML/jax.js

Herein, we present an unprecedented dual-module photochromic nanocluster, $[Th_6(OH)_4(O)_4(H_2O)_6](TPC)_8(HCOO)_4$ (**Th-SINAP-100**, TPC = 2,2':6',2"-terpyridine-4'-carboxylate), featuring both color and luminescence photochromism within a single material upon UV, β, and γ-ray irradiation. The strong Lewis acidity of Th^{IV} promotes the formation of a dense hexanuclear $[Th_6(OH)_4(O)_4(H_2O)_6]^{12+}$ cluster via hydrolysis and nucleation, which together with its third largest atomic number value among all naturally occurring elements, ensure large photoelectric attenuation coefficiency of affording material.[29] The photochromic transition from purple to yellow facilitates qualitative detection of ionization radiation. More significantly, the stepwise dual-emission PL modulation upon irradiation dose from purple, to blue, to cyan, and to green of **Th-SINAP-100** can be ultimately served as a visible colorimetric dosimeter, like the widely used pH strip, for radiation quantification. Moreover, the radiation dosimetry can be more accurately correlated with the RGB parameters of PL collected simply using a digital camera and graphic software.

Results

Synthesis and Molecular Structure

Solvothermal reaction of thorium nitrate, 2,2':6',2"-terpyridine-4'-carboxylic acid, and HCl in DMF affords purple crystals of **Th-SINAP-100**. Single crystal X-ray diffraction (SCXRD) reveals that **Th- SINAP-100** crystallizes in a triclinic space group $P\bar{1}$ (Table S1) and it features a 0D discrete nanocluster topology. The asymmetric unit consists of one $[Th_6(OH)_4(O)_4(H_2O)_6]^{12+}$ hexamer cluster decorated by eight TPC ligands and four formate anions (Fig. 1a). The $[Th_6(OH)_4O_4(H_2O)_6]^{12+}$ core is composed of six Th^{IV} ions bridged by four μ_3-O and four μ_3-OH groups with six capping H_2O molecules located on each vertex of the octahedron, which is similar to other hexameric actinide cluster species (Fig. S1).[30, 31] The Th^{IV} cation adopts a capped square antiprismatic geometry, within which eight O atoms are donated from carboxylic groups and one from a H_2O molecule. It is noteworthy that the Zr, Hf, and Ce analogues of **Th-SINAP-100** cannot be obtained under comparable conditions since cations in $[M_6(OH)_4O_4]^{12+}$ (M = Zr, Hf, and Ce) clusters are typically eight-coordinated without being decorated with water molecules.[32, 33] The 0D clusters are further packed via weak intermolecular van der Waals interaction and aromatic π-π stacking interactions as shown in Fig. 1b. Two neighboring TPC ligands are approximately parallel with a nearest interlamellar distance of 3.179 Å, suggesting the presence of π−π interactions between the moieties (Fig. 1c and 1d). The phase purity of bulk samples of **Th-SINAP-100** was confirmed by powder X-ray diffraction (PXRD) (Fig. S2).

Dual-Module Photochromism

Upon UV (365 nm), β-ray (1.2 MeV), or γ-ray (2.22×10^{15} Bq) irradiation, **Th-SINAP-100** exhibits photochromic transformation from purple to yellow as shown in Fig. 2a. UV and X-ray induced photochromic switching behavior is relatively common, while γ-ray responsive photochromism was [34, 35] **Th-SINAP-100** represents the first case of a material featuring a β-ray

Loading [MathJax]/jax/output/CommonHTML/jax.js

induced photochromic property reported to date. The evolution of UV-Vis adsorption spectra was initially acquired under exposure to 365 nm UV light, as depicted in Fig. 2b. The purple crystal displayed three adsorption maxima at approximately 340, 410, and 580 nm. The bands at 340 nm diminished gradually as a function of irradiation dose, while the intensities of the peaks at 410 and 580 nm increased and maximized after 0.04 mJ UV radiation (Fig. 2b). Upon further irradiation, two peaks at short wavelength area (340 and 410 nm) slowly merged into a broad band and the one at 580 nm was diminished, which can be considered as the second stage (Fig. 2b, inset). Similar spectral evolutions upon β- and γ-ray irradiation were observed for **Th-SINAP-100** as shown in Fig. S3. One should note that the TPC ligand did not show obvious photoinduced color change even after 38.09 mJ UV radiation, which is consistent with its negligible variation of UV-Vis spectra upon irradiation (Fig. S4).

More strikingly, **Th-SINAP-100** exhibits an extremely rare luminescence photochromism with PL color evolution upon continuous UV, β-ray, and γ-ray irradiations (Fig. 2c and S5). Such PL modulations upon exposure to external stimuli have only been documented in [((PyrO)$_3$tacn)Gd(THF)] and Pb(2-MTA)DMF (SCU-200).[18, 36] Moreover, single material featuring dual-module color and luminescence photochromism is unprecedented. Explicitly, nonirradiated **Th-SINAP-100** displayed blue emission under excitation with 365 nm light, corresponding to the broad PL maxima at 432 nm in its PL spectrum (Fig. 2d, inset). The intensity of PL_{432} drastically decreased as a function of exposure time and approximately 8% of the original intensity preserved upon 0.04 mJ UV irradiation. This photo bleaching process can be correlated with the first stage of photochromism, wherein the absorption at 340 nm is suppressed. Further UV irradiation resulted in the emergence of a broad PL band centered at 532 nm and this change can be seen by gradate transitions of the emission color from blue, to cyan, and eventually to green (Fig. 2d). The intensity of the PL_{532} band is saturated after 4.21 mJ UV exposure and is significantly higher than the initial blue emission band. Similar phenomenon was observed when **Th-SINAP-100** was exposed to increasing doses of β- and γ-ray irradiation as shown in Fig. S5. Importantly, the **Th-SINAP-100** and TPC ligand exhibits completely different luminescence features, within which the later one experiences a decoloration process (Fig. S6).

Fluorometric Dosimeter

The coloration information can be stored and the PL intensity of **Th-SINAP-100** remained unchanged for at least 48 h when kept in dark under ambient condition, implying the potential use of **Th-SINAP-100** as a radiation dosimeter (Fig. S7). The UV radiation dosage can be simply estimated by the PL color from the observation by the naked eyes and more accurately correlated with the CIE chromaticity coordinate as a numerical representation (Fig. 3a and Table S2). Alternatively, the unique ratiometric dual-emission with opposite PL dependence on dose could be utilized for detection of radiation with higher accuracy. This type of spectroscopic character has been employed for the efficient sensitization of cation species, but was for the first time applied for quantification of ionization radiation.[37] The inclusion of an addition emission band as a reference not only allows fine-tuning the energy transfer via photo-activation, but also eliminates possible interference, e.g. drift of the light resource and detector, to improve detection accuracy.[37] The declined intensity of PL at 432 nm and inclined emission band at 532 nm contribute to

Loading [MathJax]/jax/output/CommonHTML/jax.js

the continuous increase of I_{532}/I_{432} ratio as a function of irradiation dose. Linear correlations with three distinct slopes between the PL intensity ratios of I_{532}/I_{432} and the UV doses can be established as shown in Fig. 3b, leading to an accurate UV detection over a broad dose ranging from 0 – 4.2 mJ. The sharper transition of I_{532}/I_{432}, at a low dose region compared to those of I_{532} and I_{432}, suggests more accurate dose detection and less interference.

Direct Readout Colorimetric Dosimeter

Promoted by the stepwise luminescence photochromism of **Th-SINAP-100** from purple, to blue, to cyan, and to green upon γ-ray radiation, a colorimetric dosimeter for visible quantification of irradiation dose without a separate readout apparatus was developed. **Th-SINAP-100** was sealed in a customized quartz slide as a carry-on dosimeter with a small dimension of 2 × 2 cm^2 (Fig. 3c). **A** color matching chart was prepared by exposing **Th-SINAP-100** to γ-ray irradiations with precisely controlled doses and can be utilized as a reference for unknown doses. As shown in Fig. 3d, **Th-SINAP-100** exhibits eight distinct PL colors in response to 1, 3, 5, 7, 10, 30, 50, and 80 kGy γ-ray irradiation, while the color remains unchanged when the dose is further increased to 100 kGy. The upper limit of radiation dose is approximately 80 kGy, which is superior to all existing radio-photoluminescence dosimeters, e.g. Pb(2-MTA)·DMF (SCU-200) and LiF:Mg (TLD-100).[18, 38] The dose range of **Th-SINAP-100** is comparable to commercialized radiochromic film dosimeter GEX B3 and among one the highest of all dosimeters. [13, 39] This feature makes **Th-SINAP-100** particularly suitable for high dose (kGy level) monitoring in diverse fields including synchrotron radiation monitoring, food processing, radiodegration, and medical sterilization.[40, 41] The operation ranges of tranditional metal-ion-doped inorganic dosimeters, e.g. Ag-doped phosphate glass and Mg^{2+}-doped LiF (LiF:Mg), are saturated at realatively low dose due to their limited number of PL metal centers.[42] In contrast, the larger set of radiation sensitive organic linkers in metal-organic materials allows for a higher saturation point and a wider operation range. Furthermore, **Th-SINAP-100** offers substantial advantages over traditional radiation dosimeters, e.g. film badge, quartz fiber, Geiger tube, metal–oxide–semiconductor field-effect transistor (MOSFET) dosimeter, and TLD, in terms of onsite analysis, direct readout, user-friendly, low cost, or portability.

More gratifyingly, the RGB components can be extracted from the PL by simply capturing and analyzing the optical image using a digital camera and graphic software, respectively (Fig. 3e). The green (G) component of the three primary colors (RGB) as a function of γ-ray irradiation dose was plotted as shown in Fig. 3b. Two regions of good linear responses with R^2 values of 0.989 and 0.997 were established in the ranges of 1–10 kGy and 10–80 kGy, respectively (Fig. 3f). This quantitative colorimetric analysis based on a RGB scale leads to more accurate radiation dosimetry over such ranges.

Radiolytic Stability.

The radiolytic stability of **Th-SINAP-100** was examined by exposing polycrystalline **Th-SINAP-100** under β and γ-rays with dose rates of 150 kGy/h and 11.8 kGy/h, respectively. The structure of **Th-SINAP-100** remained unchanged even after 1 MGy dose of both β and γ-ray irradiation, as evidenced by their

Loading [MathJax]/jax/output/CommonHTML/jax.js

corresponding PXRD patterns and FTIR spectra (Fig. 4 and Fig. S8). Metal-organic frameworks (MOFs) featuring high radioresistance were known and $Th_6O_4(OH)_4(H_2O)_6(C_{22}O_6H_{12})_6$ (TOF-16) represents the most radioresistant MOFs reported to date (Table S3).[43] The investigation on radiation stability of cluster species was conducted for the first time in this work and the only relevant case is an ultrastable [Hf_{13}] nanocluster which is highly resistant to both concentrated acid and alkali.[44, 45] **Th-SINAP-100** represents the only reported radioresistant polynuclear cluster and one of the most radioresistant metal-organic materials in general. This outstanding radiolytic stability could be attributed to the conjugated π-electrons of terpyridine to stabilize the organic linkers and the affording cluster.[46] The strong π−π interactions between the neighboring terpyridine moieties further stabilize the metal clusters. Furthermore, thermogravimetric analysis (TGA) demonstrated that **Th-SINAP-100** exhibits a decent thermal stability, which is stable up to 150 °C (Fig. S9).

Mechanism of Photochromism and Photoluminescence Modulation

The photochromism can be explained by a variety of mechanisms, including phase transitions,[47] generation of radical species,[48] electron-transfer (redox) chemical process,[49] tautomeric shift,[50] photoinduced charge transfer (PET), etc.[51] To gain insight into the photocoloration mechanism of **Th-SINAP-100**, the PXRD patterns and FTIR spectra before and after irradiation were collected, showing no obvious variations of structure and chemical constituent (Fig. 4 and Fig. S8). The recorded electron paramagnetic resonance (EPR) spectra indicate that **Th-SINAP-100** is EPR silent before irradiation but shows a sharp resonance after UV-, β-ray, and γ-ray irradiation at g = 2.0044, corresponding to the tensor value (g = 2.0023) of a free electron (Fig. 5a).[25] The PL intensity of **Th-SINAP-100** remains approximately unchanged after removal of continuous radiation source, suggesting that the affording radicals are stable under ambient conditions (Fig. S7). These observations led to the tentative speculation that the photochromism and PL modulation of **Th-SINAP-100** originate from the generation of radical species. However, neither photochromism nor similar PL modulation was observed for a pure TPC ligand despite the fact that radical species (g = 1.9166 in EPR) can be identified (Fig. S10), implying an alternative mechanism to elucidate these unusual photoresponsive properties.

To further elucidate the photochromic behavior of **Th-SINAP-100**, we resort to density functional theory (DFT) calculations. Experimentally synthesized **Th-SINAP-100** (abbreviated as **TS**) and two groups of simplified complex models, $[Th_6(OH)_4(O)_4(H_2O)_6](TPC)$ (**TS-m**) and $[Th_6(OH)_4(O)_4(H_2O)_6](TPC)_2$ (**TS-d**), were fully optimized (Fig. 5b). **TS-m1** and **TS-d1** were found to be the most energetically stable states among their respective isomers. The computed Th − O distances exhibit the order of $Th - O_{oxo/hydroxo} < Th - O_{TPC} \approx Th - O_{HCOO} < Th - O_W$, whose values agree well with the experimental ones (Table S4 and S5). Furthermore, their bond orders range from 0.34 to 0.80, indicating weak single bond character between Th^{IV} and oxo atoms (Table S6).

Time-dependent DFT calculations (TD-DFT) were carried out by using the most stable **TS-d1** model. The experimental intense absorption at 340 nm is comparable to the theoretically simulated one at 360 nm unction unraveled that the band arises from the π(TPC)→π*

Loading [MathJax]/jax/output/CommonHTML/jax.js

(TPC) intramolecular charge transfer (laMCT) mixed with a partial contribution of the thorium-oxo moiety. It is intuitively supported by the orbitals involved in the 364 nm transition with the largest oscillator strength (Fig. 5c). Additionally, a relatively low-energy transition was calculated at 392 nm and its virtually transition-forbidden nature implies very slight contribution to the experimental 410 nm peak (Fig. S11). Given the limitation of single-cluster models, the calculations of **TS-d1** and **TS-m1** did not yield absorptions that could be comparable to experimental peaks at longer wavelengths (410 and 580 nm) (Fig. 2b).

To gain a deeper insight into the mechanism of photocoloration, detailed structural comparisons were performed on a single crystal of **Th-SINAP-100** before and after the γ-ray irradiated with an accumulated dose of 200 kGy. Both datasets were collected under identical conditions including temperature, measurement angles, and exposure time. SCXRD studies revealed that the overall topologies before and after irradiation remain unchanged, whereas the unit cell parameters *a*, *b*, *c*, and *V* shrink from 14.526(1) Å, 17.246(2) Å, 18.504(2) Å, and 3908.7(6) $Å^3$ to 14.500(6) Å, 17.173(7) Å, 18.368(9) Å, and 3875.0(3) $Å^3$, respectively, implying a more compact molecular packing after irradiation (Table S1).[52] Concomitantly, the interplane distances of the π-π stacking of the terpyridyl rings along the *c* axis decrease from 3.179 to 3.155 Å (Fig. 1d). These π-π interactions are enhanced allowing π→π* transition to occur between adjacent TPC ligands, which enables intermolecular charge transfer (leMCT) and eventually gives rise to the absorption bands at 410 and 580 nm for **Th-SINAP-100**.

In brief, the high-energy experimental band (340 nm) is attributable to laMCT in nature, while the two lower-energy ones (410 and 580 nm) are primarily of leMCT. More detailed results from TD-DFT calculations show that the absorption band at 410 nm features a negligible laMCT mixture. Moreover, TPC precursor does not exhibit photochromism owing to the lack of such π-π stacking interactions. The luminescence photochromism of **Th-SINAP-100** was further rationalized by DFT calculations. The assembly of Th^{IV} and TPC ligands into the molecular complex facilitates the π-π stacking of TPC moieties in the crystalline environment. Consequently, two types of excited states, **TS*** originating from laMCT and (**TS**-**TS**)* from leMCT, can be created under excitation. Since being stabilized by the charge transfer, the excimer (**TS**-**TS**)* is lower in energy than the discrete **TS***+**TS**, corresponding to an emission band at longer wavelength region (532 nm vs. 432 nm) (Fig. 5d).

Discussion

We have developed an unprecedented case of a dual-module photochromic metal-organic nanocluster, **Th-SINAP-100**, that delivers direct readout colorimetric dosimetry for UV and ionizing radiations. The combination of dense $[Th_6(OH)_4(O)_4(H_2O)_6]^{12+}$ cores as radiation attenuators and the TPC ligands as photo-responsive sensors gives rise to extremely rare both color and luminescence photochromic transitions incorporated into a single material. To our best knowledge, **Th-SINAP-100** represents the only case of a known β-ray induced photochromic material. The striking and visible response of PL allows **Th-SINAP-100** to function as a colorimetric dosimeter for ionizing radiations, like the widely used pH stripe,

Loading [MathJax]/jax/output/CommonHTML/jax.js

overcoming the reliance on readout instruments for radiation dosimetry. Thanks to the high density of radiation sensitive organic linkers in its structure, a record high dose (1 MGy) of dosimetry among all existing radio-photoluminescence materials have been achieved. SCXRD studies and DFT/TD-DFT calculations revealed that the enhanced π-π stacking interaction between the adjacent TPC moieties upon irradiation results in the IaMCT→IeMCT conversion, which ultimately leads to the unusual photoinduced peculiarities.

Methods

Caution! Th-232 used in this study is an α emitter with the daughter of radioactive Ra-228. All of the thorium compounds used and investigated were operated in an authorized laboratory designed for actinide element studies. Standard protections for radioactive materials should be followed.

Materials.

$Th(NO_3)_4·6H_2O$ (99.9%, Changchun Institute of Applied Chemistry, Chinese Academy of Sciences), 2,2':6',2"-terpyridine-4'-carboxylic acid (HTPC) (99%, Jilin Chinese Academy of Sciences - Yanshen Technology Co., Ltd), DMF (99.5%, Aladdin), and HCl (AR, 36 ~ 38%, Sinopharm Chemistry Reagent Co., Ltd) were used as received from commercial suppliers without further purification.

Synthesis

A mixture of $Th(NO_3)_4·6H_2O$ (29.4 mg, 0.05 mmol), HCl (100 μL), 2,2':6',2"-terpyridine-4'-carboxylic acid (13.8 mg, 0.05 mmol), DMF (1 mL), and deionized water (1 mL) were loaded into a 5 mL vials. The vial was sealed and heated to 100 °C for 24 h and then cooled to room temperature under ambient condition. Light purple block crystals of **Th-SINAP-100** were isolated after being washed with deionized water and allowed to air-dry at room temperature.

Crystallographic analysis

Single crystal X-ray diffraction measurements were performed using a Bruker D8-Venture single crystal X-ray diffractometer equipped with a Turbo X-ray Source (Mo–Kα radiation, λ = 0.71073 Å) and a CMOS detector at 298 K. The data frames were collected using the program *APEX3* and processed using the program *SAINT* routine in *APEX3*. The structures were solved by the direct method and refined on F^2 by full-matrix least-squares methods using *SHELXTL-2014* program.[1] Powder X-ray diffraction (PXRD) data were collected from 5 to 50° with a step of 0.02° and the time for data collection was 0.5 s on a Bruker D8 Advance diffractometer with Cu Kα radiation (λ = 1.54056 Å) and a Lynxeye one-dimensional detector.

Physical Property Measurements

The solid-state UV-Vis absorption and photoluminescence spectra were recorded on a Craic Technologies microspectrophotometer. Crystals were placed on quartz slide, and data was collected after auto-set optimization. When the 365 nm excitation light was selected, an optical filter masking signal below

Loading [MathJax]/jax/output/CommonHTML/jax.js

erference of excitation light. The IR spectra were recorded

using a FTIR spectrometer (Thermo Nicolet 6700 spectrometer) equipped with a diamond attenuated total reflectance (ATR) accessory in the range of 400–4000 cm^{-1}. Thermalgravimetric analysis was carried out on a NETZSCH STA 449 F3 jupiter instrument in the range of 30–900 °C under a nitrogen flow at a heating rate of 10 °C/ min. The electron paramagnetic resonance (EPR) data for nonirradiated and irradiated samples was recorded with a Bruker EMXplus 10/12 EPR spectrometer equipped with an Oxford Instruments EPR901 liquid helium continuous-flow cryostat fitted with a super-high-Q cavity. The magnetic field was measured by a Hall probe calibrated with the 1,3-bisdiphenylene-2-phenylallyl EPR signal and a Bruker ER 036TM teslameter. The microwave frequency was measured with an internal frequency counter. The temperature was controlled with an Oxford Instruments ITC503S temperature controller. The spectra were acquired with a sweep width of 500 G, a frequency of 9.404789 GHz, a modulation amplitude of 2 G, a modulation frequency of 100 kHz, and at temperature of 293 K.

Radiation-Resistance Measurements

The radiation-resistant properties were examined by irradiating of **Th-SINAP-100** with β-ray and γ-ray. The sources of β-ray and γ-ray were provided by an electron accelerator (1.2 MeV) and a ^{60}Co irradiation source (2.22×10^{15} Bq), respectively. **Th-SINAP-100** was irradiated with two different doses (200 kGy and 1 MGy) with dose rates of 150 and 11.8 kGy/h for β-ray and γ-ray, respectively. PXRD and FTIR analyses on the irradiated samples were performed to confirm the radiation-resistance of **Th-SINAP-100.**

Computational Method

Density functional theory (DFT) calculations were performed to optimize the structure of the experimentally obtained **Th-SINAP-100** (abbreviated as **TS**). The inclusion of 300 atoms and 2278 electrons within this large molecular complex results in high computational demand to elucidate the electronic structure, particularly excited states, of **Th-SINAP-100**. Therefore, the complex was simplified by replacing bulky TPC ligand with CH_3COO^- moiety as shown in Fig. 5b. Consequently, two simplified complex modes, **TS** monomer (**TS-m**) and dimer (**TS-d**), which feature one and two TPC ligands in the molecule respectively, were selected. The possible isomers were optimized for both modes and the structures of the most energetically stable isomers were depicted in Fig. 5b.

In geometry optimizations, the PBE functional of the generalized gradient approximation (GGA) was applied. A scalar relativistic four-component all-electron approach and all-electron correlation-consistent double-ς polarized quality basis sets were used.[53] Subsequent analytical frequency calculations were used to confirm the nature of the stationary points on the potential energy surface.[53] The zero-point vibrational energy (ZPVE) and entropy were further obtained. Population-based Mayer[3] bond orders and Mulliken charges were calculated. All these calculations were accomplished with the Priroda code.[53, 54]

The electronic structures were calculated with the ADF 2014 code while employing the above optimized **TS-m1** and **TS-d1** geometries.[55, 56, 57] An integration parameter of 6.0 was applied. The ZORA scalar relativistic approach of van Lenthe et al was employed, associated with the Slater-type TZP basis sets.[58, 59, 60, 61] The time-dependent density functional theory (TD-DFT) with the PBE functional was performed to

Loading [MathJax]/jax/output/CommonHTML/jax.js

calculate electronic absorption spectra. Fifty spin-allowed excited states were calculated for model complexes, and eighty ones for the TPC ligand. Considering the effect of the environmental media on above properties, we used the Conductor-Like Screening Model (COSMO)[62, 63] to simulate the crystalline environment surrounding the complex. The solvent water was utilized with the dielectric constant of 78.38. Klamt radii were used for the main group atoms (H = 1.30 Å, C = 2.00 Å, O = 1.72 Å and N = 1.83 Å) and for the thorium atom (2.00 Å).[64, 65, 66]

End Notes

Acknowledgments. This work was supported by the National Natural Science Foundation of China (21701184, 21790374, 21876182, 21825601, and 22076196), the Strategic Priority Research Program of the Chinese Academy of Sciences (XDA21000000), and the K.C.Wong Education Foundation (GJTD-2018-10).

Declarations

Acknowledgments. This work was supported by the National Natural Science Foundation of China (21701184, 21790374, 21876182, 21825601, and 22076196), the Strategic Priority Research Program of the Chinese Academy of Sciences (XDA21000000), and the K.C.Wong Education Foundation (GJTD-2018-10).

Author contributions. J.L. conceived and supervised the project. H.L designed and synthesized the material. H.L., J.X., and Y.W. carried out the characterizations and analyzed the data. Z.L. aided in the irradiation experiments. X.W. and Q.P. carried out the theoretical calculation. H.L., K.D., Q.P., S.W., J.W., and J.L. wrote the paper. All authors discussed the results and commented on the manuscript.

Additional information. Supplementary information is available in the online version of the paper. Correspondence and requests for materials should be addressed to linjian@sinap.ac.cn (Jian Lin), shuaowang@suda.edu.cn (Shuao Wang), or panqjitc@163.com (Qing-Jiang Pan).

Competing Financial Interests statement. A patent “Metal-organic hybrid material for ionization radiation dosimetry, 202010501386X.” on the related content has been filed by Jian-Qiang Wang, Huangjie Lu, Jian Lin, and Shanghai Institute of Applied Physics, Chinese Academy of Sciences. The remaining authors declare no competing interests.

References

1. Tao, Y., Li M., Liu X., Leong K.W., Gautier J., Zha S. Dual-Color Plasmonic Nanosensor for Radiation Dosimetry. *ACS Appl. Mater. Interfaces* **12**, 22499–22506 (2020).
2. Xie, J.*, et al.* Highly Sensitive Detection of Ionizing Radiations by a Photoluminescent Uranyl Organic Framework. *Angew. Chem. Int. Ed.* **56**, 7500-7504 (2017).

Loading [MathJax]/jax/output/CommonHTML/jax.js

3. Li, X., *et al.* Three-Dimensional Lead Iodide Perovskitoid Hybrids with High X-ray Photoresponse. *J. Am. Chem. Soc.* **142**, 6625–6637 (2020).
4. Thirimanne, H.M., *et al.* High sensitivity organic inorganic hybrid X-ray detectors with direct transduction and broadband response. *Nat. Commun.* **9**, 2926 (2018).
5. Wei, H., Huang J. Halide lead perovskites for ionizing radiation detection. *Nat. Commun.* **10**, 1066 (2019).
6. Zhang, Y., *et al.* Nucleation-controlled growth of superior lead-free perovskite $Cs_3Bi_2I_9$ single-crystals for high-performance X-ray detection. *Nat. Commun.* **11**, 2304 (2020).
7. Knoll, G.F. *Radiation Detection and Measurement*. Wiley (2010).
8. Liang, C., *et al.* Thermoplastic Membranes Incorporating Semiconductive Metal-Organic Frameworks as a New Generation of Flexible X-ray Detectors. *Angew. Chem. Int. Ed.* **59**, 11856–11860 (2020).
9. Morad, V., Shynkarenko Y., Yakunin S., Brumberg A., Schaller R.D., Kovalenko M.V. Disphenoidal Zero-Dimensional Lead, Tin, and Germanium Halides: Highly Emissive Singlet and Triplet Self-Trapped Excitons and X-ray Scintillation. *J. Am. Chem. Soc.* **141**, 9764-9768 (2019).
10. Wang, Y., *et al.* Direct Radiation Detection by a Semiconductive Metal–Organic Framework. *J. Am. Chem. Soc.* **141**, 8030-8034 (2019).
11. Chen, Q., *et al.* All-inorganic perovskite nanocrystal scintillators. *Nature* **561**, 88-93 (2018).
12. Kim, Y.C., *et al.* Printable organometallic perovskite enables large-area, low-dose X-ray imaging. *Nature* **550**, 87-91 (2017).
13. Butson, M.J., Yu P.K.N., Cheung T., Metcalfe P. Radiochromic film for medical radiation dosimetry. *Mater. Sci. Eng. R Rep.* **41**, 61-120 (2003).
14. Devic, S., Tomic N., Lewis D. Reference radiochromic film dosimetry: Review of technical aspects. *Phys. Med.* **32**, 541-556 (2016).
15. Stavila, V., Talin A.A., Allendorf M.D. MOF-based electronic and opto-electronic devices. *Chem. Soc. Rev.* **43**, 5994-6010 (2014).
16. Allendorf, M.D., Bauer C.A., Bhakta R.K., Houk R.J.T. Luminescent metal–organic frameworks. *Chem. Soc. Rev.* **38**, 1330-1352 (2009).
17. Kreno, L.E., Leong K., Farha O.K., Allendorf M., Van Duyne R.P., Hupp J.T. Metal–Organic Framework Materials as Chemical Sensors. *Chem. Rev.* **112**, 1105-1125 (2012).
18. Liu, H., *et al.* Emergence of Radical-Stabilizing Metal-Organic Framework as a New Type of Radio-Photoluminescence Dosimeter. *Angew. Chem. Int. Ed.* **59**, 1-7 (2020).
19. Wang, Y., *et al.* Emergence of Uranium as a Distinct Metal Center for Building Intrinsic X-ray Scintillators. *Angew. Chem. Int. Ed.* **57**, 7883–7887 (2018).
20. Tang, S., *et al.* Tunable Reduction of 2,4,6-Tri(4-pyridyl)-1,3,5-Triazine: From Radical Anion to Diradical Dianion to Radical Metal–Organic Framework. *Angew. Chem. Int. Ed.* **58**, 18224 –18229 (2019).

Loading [MathJax]/jax/output/CommonHTML/jax.js

21. Hu, K.-Q., *et al.* Solar-Driven Nitrogen Fixation Catalyzed by Stable Radical-Containing MOFs: Improved Efficiency Induced by a Structural Transformation. *Angew. Chem. Int. Ed.*, DOI: 10.1002/anie.202009630.
22. Zhang, X., Wang M.-S., Sun C., Yang C., Li P.-X., Guo G.-C. Stabilizing and color tuning pyrazine radicals by coordination for photochromism. *Chem. Commun.* **52**, 7947-7949 (2016).
23. Xu, G., Guo G.-C., Wang M.-S., Zhang Z.-J., Chen W.-T., Huang J.-S. Photochromism of a Methyl Viologen Bismuth(III) Chloride: Structural Variation Before and After UV Irradiation. *Angew. Chem. Int. Ed.* **46**, 3249-3251 (2007).
24. Koshima, H., Ojima N., Uchimoto H. Mechanical Motion of Azobenzene Crystals upon Photoirradiation. *J. Am. Chem. Soc.* **131**, 6890-6891 (2009).
25. Wang, M.-S., *et al.* A Room-Temperature X-ray-Induced Photochromic Material for X-ray Detection. *Angew. Chem. Int. Ed.* **51**, 3432-3435 (2012).
26. Chen, C., Sun J.-K., Zhang Y.-J., Yang X.-D., Zhang J. Flexible Viologen-Based Porous Framework Showing X-ray Induced Photochromism with Single-Crystal-to-Single-Crystal Transformation. *Angew. Chem. Int. Ed.* **56**, 14458-14462 (2017).
27. Guo, P.-Y., Sun C., Zhang N.-N., Cai L.-Z., Wang M.-S., Guo G.-C. An inorganic–organic hybrid photochromic material with fast response to hard and soft X-rays at room temperature. *Chem. Commun.* **54**, 4525-4528 (2018).
28. Han, J.-M., *et al.* Low Dose Detection of γ Radiation via Solvent Assisted Fluorescence Quenching. *J. Am. Chem. Soc.* **136**, 5090-5096 (2014).
29. Dolgopolova, E.A., Rice A.M., Shustova N.B. Actinide-based MOFs: a middle ground in solution and solid-state structural motifs. *Chem. Commun.* **54**, 6472-6483 (2018).
30. Dolgopolova, E.A., *et al.* Multifaceted Modularity: A Key for Stepwise Building of Hierarchical Complexity in Actinide Metal–Organic Frameworks. *J. Am. Chem. Soc.* **139**, 16852-16861 (2017).
31. Ejegbavwo, O.A., *et al.* Thermodynamics and Electronic Properties of Heterometallic Multinuclear Actinide-Containing Metal–Organic Frameworks with “Structural Memory”. *J. Am. Chem. Soc.* **141**, 11628-11640 (2019).
32. Wang, X., *et al.* Vanadium Catalyst on Isostructural Transition Metal, Lanthanide, and Actinide Based Metal–Organic Frameworks for Alcohol Oxidation. *J. Am. Chem. Soc.* **141**, 8306-8314 (2019).
33. Lyu, J., *et al.* Exploring the Role of Hexanuclear Clusters as Lewis Acidic Sites in Isostructural Metal–Organic Frameworks. *Chem. Mater.* **31**, 4166-4172 (2019).
34. Shen, W., Baccaro S., Cemmi A., Xu X., Chen G. Gamma-ray irradiation induced bulk photochromism in WO_3–P_2O_5 glass. *Nuclear Instruments and Methods in Physics Research Section B: Beam Interactions with Materials and Atoms* **362**, 34-37 (2015).
35. Ren, J., Xu X., Shen W., Chen G., Baccaro S., Cemmi A. Gamma-ray induced reversible photochromism of Mn^{2+} activated borophosphate glasses. *Sol. Energy Mater. Sol. Cells* **143**, 635-639 (2015).

Loading [MathJax]/jax/output/CommonHTML/jax.js

36. Nakai, H.*, et al.* Reversible Switching of the Luminescence of a Photoresponsive Gadolinium(III) Complex. *Angew. Chem. Int. Ed.* **52**, 8722-8725 (2013).
37. Liu, W.*, et al.* Ratiometric Monitoring of Thorium Contamination in Natural Water Using a Dual-Emission Luminescent Europium Organic Framework. *Environ. Sci. Technol.* **53**, 332-341 (2019).
38. Nandha Gopal, J., Sanyal B., Lakshmanan A. Radiophotoluminescence and thermoluminescence characteristics of undoped and Mg doped LiF phosphor in the high dose region. *Radiat. Meas.* **109**, 24-34 (2018).
39. Ravotti, F. Dosimetry Techniques and Radiation Test Facilities for Total Ionizing Dose Testing. *IEEE Transactions on Nuclear Science* **65**, 1440-1464 (2018).
40. *Techniques for High-Dose Dosimetry in Industry, Agriculture and Medicine - Proceedings of a symposium held in Vienna, 9-13 November 1998*. INTERNATIONAL ATOMIC ENERGY AGENCY (1999).
41. Quero, G.*, et al.* A novel Lab-on-Fiber Radiation Dosimeter for Ultra-high Dose Monitoring. *Sci. Rep.* **8**, 17841 (2018).
42. Nakamura, F., Kato T., Okada G., Kawaguchi N., Fukuda K., Yanagida T. Scintillation, TSL and RPL properties of MgF_2 transparent ceramic and single crystal. *Ceram. Int.* **43**, 7211-7215 (2017).
43. Gilson, S.E.*, et al.* Unprecedented Radiation Resistant Thorium-Binaphthol MOF. *J. Am. Chem. Soc.* **142**, 13299–13304 (2020).
44. Kang, X.-M.*, et al.* An Ultrastable Matryoshka [Hf_{13}] Nanocluster as a Luminescent Sensor for Concentrated Alkali and Acid. *Angew. Chem. Int. Ed.* **58**, 16610-16616 (2019).
45. Mei, L.*, et al.* Actinide Separation Inspired by Self-Assembled Metal–Polyphenolic Nanocages. *J. Am. Chem. Soc.*, DOI: 10.1021/jacs.1020c08048 (2020).
46. Kataoka, Y., Kanbayashi N., Fujii N., Okamura T.-a., Haino T., Onitsuka K. Construction of Helically Stacked π-Electron Systems in Poly(quinolylene-2,3-methylene) Stabilized by Intramolecular Hydrogen Bonds. *Angew. Chem. Int. Ed.* **59**, 10286-10291 (2020).
47. Kida, N.*, et al.* Control of Charge Transfer Phase Transition and Ferromagnetism by Photoisomerization of Spiropyran for an Organic–Inorganic Hybrid System, (SP)[$Fe^{II}Fe^{III}(dto)_3$] (SP = spiropyran, dto = $C_2O_2S_2$). *J. Am. Chem. Soc.* **131**, 212-220 (2009).
48. Roy, S., Mondal S.P., Ray S.K., Biradha K. A Photoswitchable and Photoluminescent Organic Semiconductor Based On Cation–π and Carboxylate–Pyridinium Interactions: A Supramolecular Approach. *Angew. Chem. Int. Ed.* **51**, 12012-12015 (2012).
49. Wang, M.-S.*, et al.* Photochromism of a 3D Cd^{II} Complex with Two Captured Ligand Isomers Generated In Situ from the Same Precursor. *Angew. Chem. Int. Ed.* **47**, 3565-3567 (2008).
50. Harada, J., Fujiwara T., Ogawa K. Crucial Role of Fluorescence in the Solid-State Thermochromism of Salicylideneanilines. *J. Am. Chem. Soc.* **129**, 16216-16221 (2007).
51. Cai, L.-Z., Chen Q.-S., Zhang C.-J., Li P.-X., Wang M.-S., Guo G.-C. Photochromism and oferrate at Room Temperature. *J. Am. Chem. Soc.* **137**,

Loading [MathJax]/jax/output/CommonHTML/jax.js

10882-10885 (2015).
52. Martinez, C.R., Iverson B.L. Rethinking the term “pi-stacking”. *Chem. Sci.* **3**, 2191-2201 (2012).
53. Laikov, D.N. A new class of atomic basis functions for accurate electronic structure calculations of molecules. *Chem. Phys. Lett.* **416**, 116-120 (2005).
54. Laikov, D.N., Ustynyuk Y.A. PRIRODA-04: a quantum-chemical program suite. New possibilities in the study of molecular systems with the application of parallel computing. *Russ. Chem. Bull.* **54**, 820-826 (2005).
55. te Velde, G.*, et al.* Chemistry with ADF. *J. Comput. Chem.* **22**, 931-967 (2001).
56. Fonseca Guerra, C., Snijders J.G., te Velde G., Baerends E.J. Towards an order-N DFT method. *Theor. Chem. Acc.* **99**, 391-403 (1998).
57. Baerends, E.J.*, et al. ADF, ADF2014.06; SCM,* . Vrije Universiteit: Amsterdam, The Netherlands (2014).
58. van Lenthe, E., Snijders J.G., Baerends E.J. The zero-order regular approximation for relativistic effects: The effect of spin–orbit coupling in closed shell molecules. *J. Phys. Chem.* **105**, 6505-6516 (1996).
59. van Lenthe, E., van Leeuwen R., Baerends E.J., Snijders J.G. Relativistic regular two-component Hamiltonians. *Int. J. Quantum Chem* **57**, 281-293 (1996).
60. van Lenthe, E., Baerends E.J., Snijders J.G. Relativistic total energy using regular approximations. *J. Phys. Chem.* **101**, 9783-9792 (1994).
61. van Lenthe, E., Ehlers A., Baerends E.-J. Geometry optimizations in the zero order regular approximation for relativistic effects. *J. Phys. Chem.* **110**, 8943-8953 (1999).
62. Pye, C.C., Ziegler T. An implementation of the conductor-like screening model of solvation within the Amsterdam density functional package. *Theor. Chem. Acc.* **101**, 396-408 (1999).
63. Klamt, A., Schüürmann G. COSMO: a new approach to dielectric screening in solvents with explicit expressions for the screening energy and its gradient. *J. Chem. Soc., Perkin Trans. 2*, 799-805 (1993).
64. Klamt, A., Jonas V., Bürger T., Lohrenz J.C.W. Refinement and Parametrization of COSMO-RS. *J. Phys. Chem. A* **102**, 5074-5085 (1998).
65. Shamov, G.A., Schreckenbach G. Relativistic Density Functional Theory Study of Dioxoactinide(VI) and -(V) Complexation with Alaskaphyrin and Related Schiff-Base Macrocyclic Ligands. *J. Phys. Chem. A* **110**, 9486-9499 (2006).
66. Pan, Q.-J., Schreckenbach G., Arnold P.L., Love J.B. Theoretical predictions of cofacial bis(actinyl) complexes of a stretched Schiff-base calixpyrrole ligand. *Chem. Commun.* **47**, 5720-5722 (2011).

Figures

Loading [MathJax]/jax/output/CommonHTML/jax.js

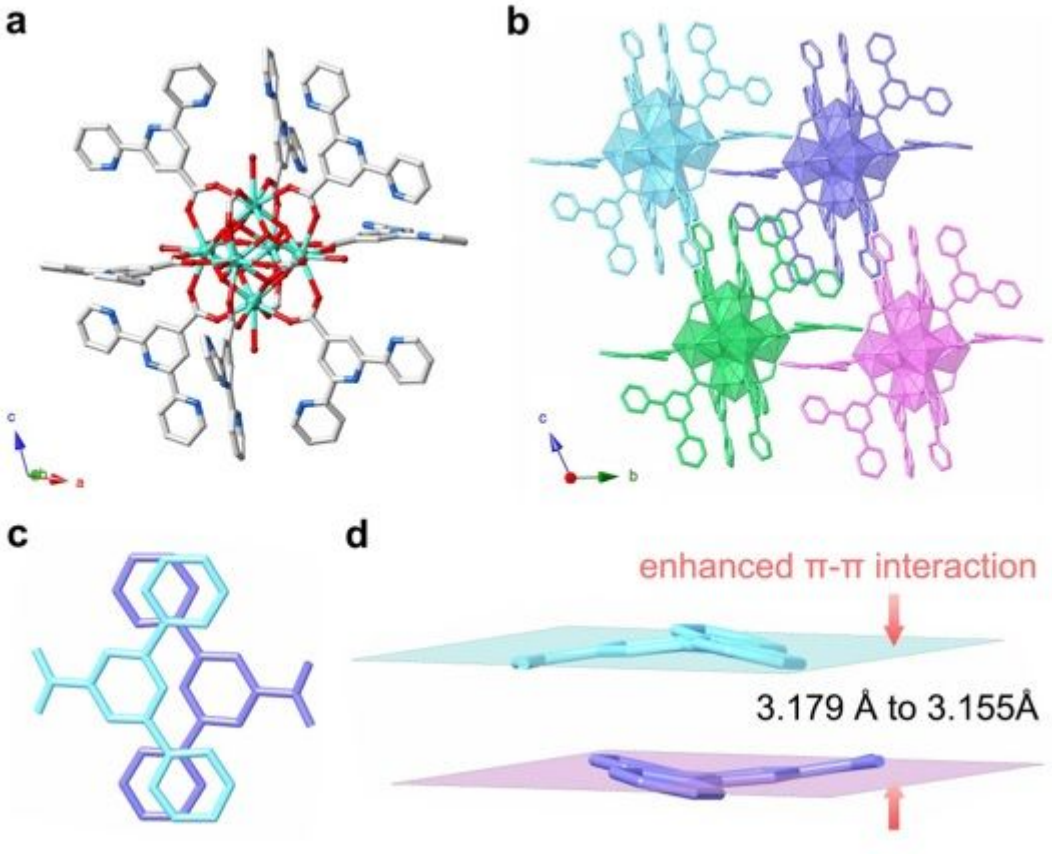


Figure 1

(a) Molecular structure of Th-SINAP-100. Color code: Th green, O red, N blue, and C gray. H atoms are omitted for clarity. (b) Topological representation of the packing of 0D clusters. (c) Top and (d) side view showing the π−π interactions in the structure of Th-SINAP-100.

Loading [MathJax]/jax/output/CommonHTML/jax.js

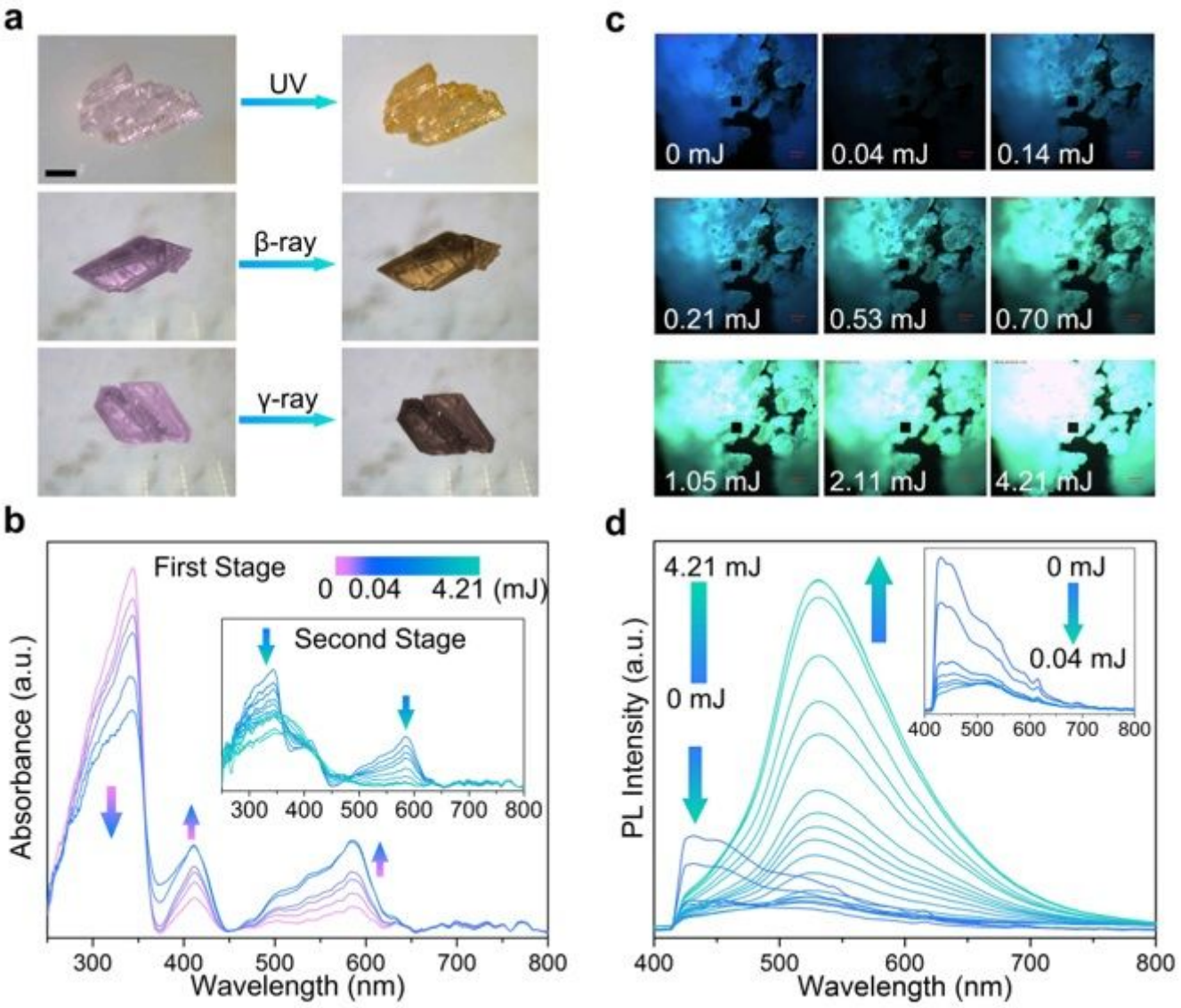


Figure 2

(a) Photochromism of Th-SINAP-100 upon UV-, β-ray, and γ-ray irradiation. (b) Evolution of the UV-Vis absorption spectra of Th-SINAP-100 after exposure to 0–0.04 mJ UV irradiation doses. Inset: UV-Vis absorption spectra of Th-SINAP-100 after exposure to 0.04–4.21 mJ UV irradiation dosse. (c) Snapshots of bulk Th-SINAP-100 crystals upon 365 nm UV irradiation. (d) Evolution of the PL spectra of Th-SINAP-100 after exposure to 0–4.21 mJ UV irradiation doses. Inset: PL spectra of Th-SINAP-100 after exposure to 0–0.04 mJ UV irradiation doses.

Loading [MathJax]/jax/output/CommonHTML/jax.js

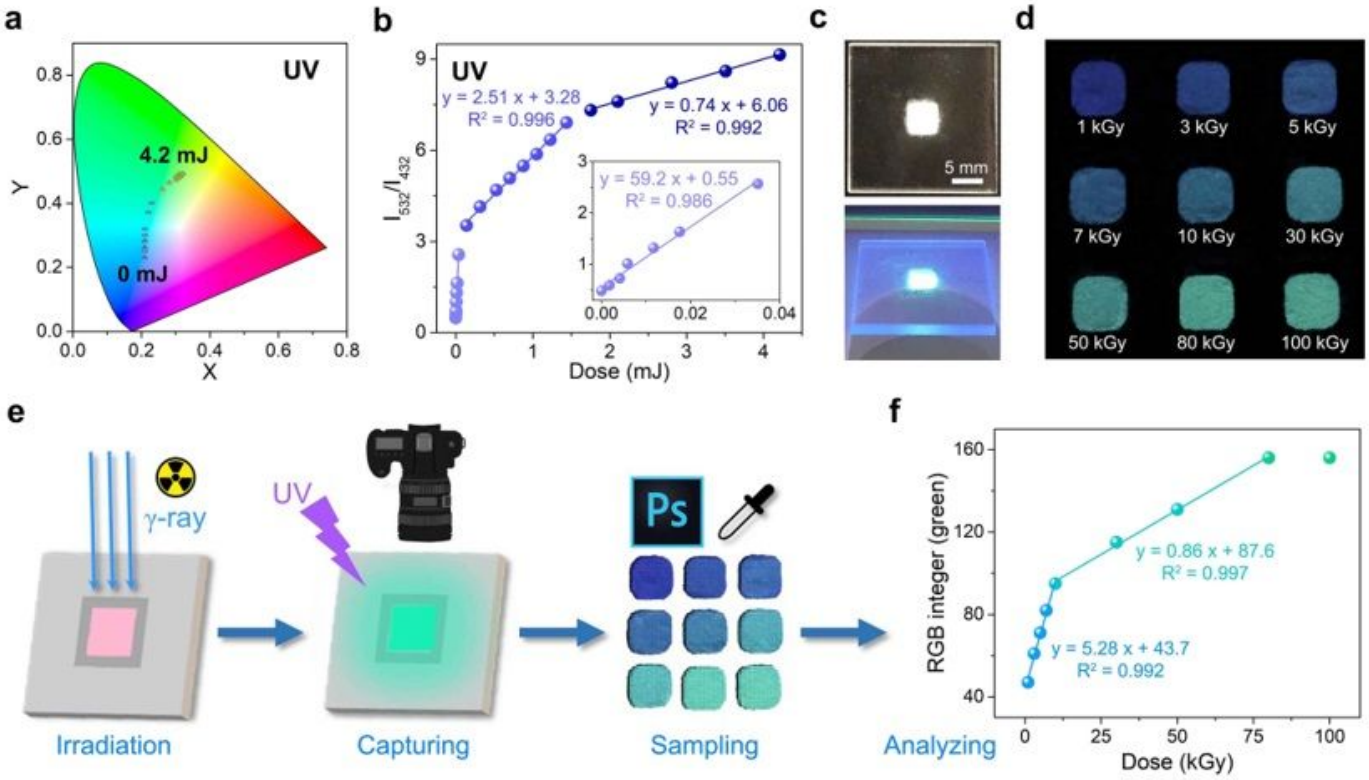


Figure 3

(a) CIE chromaticity coordinates of Th-SINAP-100 as a function of UV irradiation dose. (b) Linear fittings of the intensity ratio I532/I432 as a function of UV dosage. The inset is the linear fitting in the low dose range from 0 to 0.04 mJ. (c) Photos of Th-SINAP-100 based dosimeter. (d) Color matching chart prepared by irradiated Th-SINAP-100 with different γ-ray dose. (e) A schematic illustration of colorimetric quantification method based on RGB scale. (f) Linear fittings of the RGB integer (green) of Th-SINAP-100 as a function of γ-ray dose.

Loading [MathJax]/jax/output/CommonHTML/jax.js

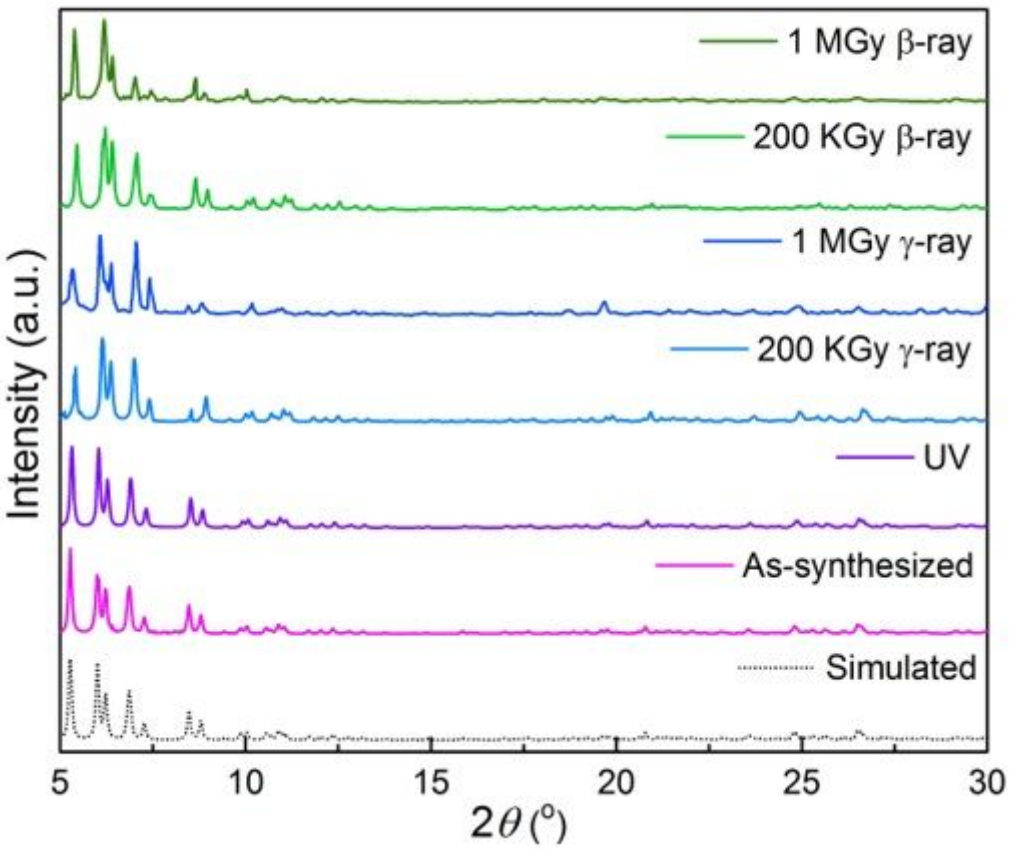


Figure 4

PXRD patterns of Th-SINAP-100 before and after irradiation with UV, β-ray, and γ-ray.

Loading [MathJax]/jax/output/CommonHTML/jax.js

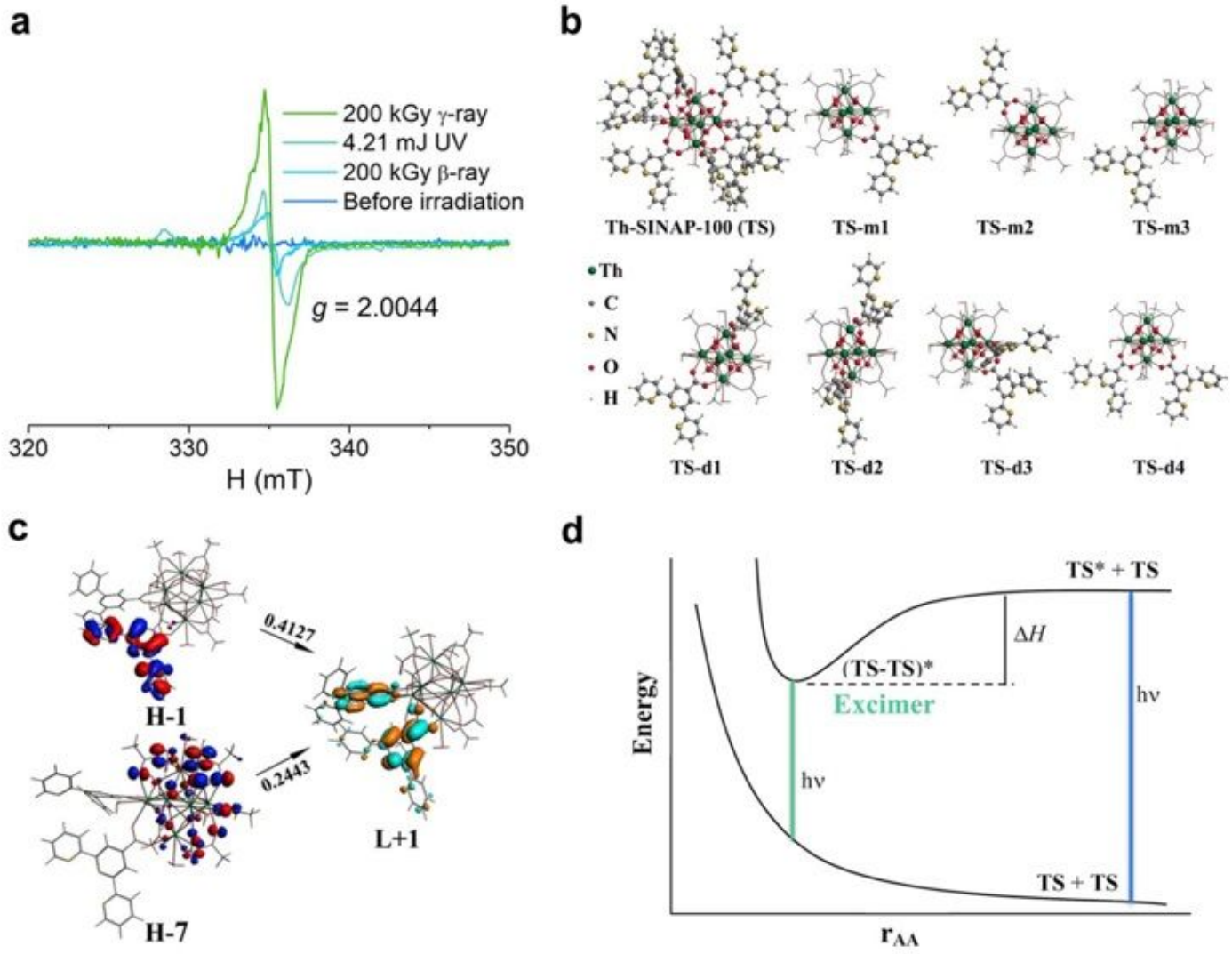


Figure 5

(a) EPR spectra of Th-SINAP-100 before and after irradiation. (b) Optimized structures of the experimentally synthesized complex and selected simplified models. (c) Orbital diagrams of the 364 nm electron transitions for TS-d1 from the TD-DFT calculations. (d) The formation of excimer (TS-TS)* that is stabilized charge transfer, along with the light emitted by (TS-TS)* and TS*+TS.

Supplementary Files

This is a list of supplementary files associated with this preprint. Click to download.

- SupportingInformationf.docx
- checkcif.pdf
- cif.cif

Loading [MathJax]/jax/output/CommonHTML/jax.js